
Multi-Camera Calibration Free BEV Representation for 3D Object Detection

Hongxiang Jiang^{1,2*} Wenming Meng² Hongmei Zhu² Qian Zhang² Jihao Yin^{1†}

¹Beihang University ²Horizon Robotics

Abstract

In advanced paradigms of autonomous driving, learning Bird’s Eye View (BEV) representation from surrounding views is crucial for multi-task framework. However, existing methods based on depth estimation or camera-driven attention are not stable to obtain transformation under noisy camera parameters, mainly with two challenges, accurate depth prediction and calibration. In this work, we present a completely Multi-Camera Calibration Free Transformer (CFT) for robust BEV representation, which focuses on exploring implicit mapping, not relied on camera intrinsics and extrinsics. To guide better feature learning from image views to BEV, CFT mines potential 3D information in BEV via our designed position-aware enhancement (PA). Instead of camera-driven point-wise or global transformation, for interaction within more effective region and lower computation cost, we propose a view-aware attention which also reduces redundant computation and promotes converge. CFT achieves 49.7% NDS on the nuScenes detection task leaderboard, which is the first work removing camera parameters, comparable to other geometry-guided methods. Without temporal input and other modal information, CFT achieves second highest performance with a smaller image input (1600×640). Thanks to view-attention variant, CFT reduces memory and transformer FLOPs for vanilla attention by about 12% and 60%, respectively, with improved NDS by 1.0%. Moreover, its natural robustness to noisy camera parameters makes CFT more competitive.

1 Introduction

3D object detection from multi-camera 2D images is a critical perception technique for autonomous driving systems with compared to expensive LiDAR-based [10, 18, 3] or multi-modal approaches [42, 41, 50, 49, 2, 30, 12]. Recent approaches emphasize transforming 2D image features to sparse instance-level [9, 37, 45] or dense Bird’s Eye View (BEV) representation [16, 22, 26], characterizing the 3D structure of the surrounding environment. Although some depth-based detectors [16, 17, 21, 26, 51] incorporate depth estimation to introduce such 3D information, the extra depth supervision is acquired for preciser detection. Therefore, other paradigms [22, 45] directly learn the transformation based on the attention mechanism [40]. They explicitly predict the 3D coordinates of queries. With these coordinates, the camera intrinsic and extrinsic parameters, local image features could be sampled to perform cross-attention, as shown in Fig. 1a. However, the obtained representation is not stable due to the inaccurate prediction, calibration error or dynamic variety of the camera parameters in real-world scenes. Inference speed also suffers from point-wise coordinate projection and sampling.

To learn representation more stably, researchers [25, 52] indirectly discover the relationship of different views by implicitly generating camera-driven 3D positional embedding. This bypasses

*This work is done when Hongxiang Jiang is an intern at Horizon Robotics.

†Jihao Yin (jihaoyin@buaa.edu.cn) is the corresponding author with the School of Aerospace, Beihang University, Beijing, China.

the position estimation, but attention computation is still sensitive to camera parameters, which is shown in Fig. 1b. In fact, the existing analysis[22, 26, 33] also shows that the noisy extrinsics have a great impact on the results. Besides, global attention between each position of the BEV grids and that of the image pixels causes high computational cost. Consequently, considering the above problems with explicit or implicit camera-driven attention, removing geometry prior for robust BEV representation and reaching a good balance between performance, speed and computational cost is of great importance.

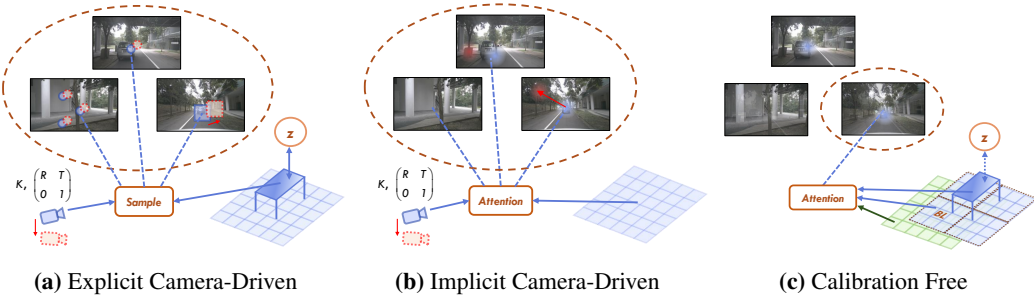


Figure 1: Illustration of our calibration free BEV representation. (a) and (b) show explicit or implicit camera-driven attention interaction, z in (a) is the true height coordinate corresponding to the predicted value of each BEV grid. Bias in camera parameter affects the learning of correct transformations. (c) is the proposed CFT, where the green and blue grids represent BEV content embedding and positional embedding, respectively, divided into 2×2 windows for view-level attention. The additional embedding of z could be obtained in a supervised or unsupervised manner, then restructured together with other embedding for attention.

In this work, we propose a multi-camera **Calibration Free Transformer (CFT)**, learning BEV representation for 3D object detection without any geometric guidance. Fig. 1c briefly illustrates our CFT, which helps the camera parameters-free translation between image views and BEV via implicitly enhancing 3D feature in the BEV embedding. Specifically, CFT proposes a content-based position-aware enhancement (PA). Thanks to PA that captures location and content separately, even implicit unsupervised learning can reliably extract 3D positional information, similar to the results of adding explicit supervision in PA. The original 2D coordinates encoding of BEV could contain richer 3D cues, gaining sufficient interaction with image pixels. This not only stably learns the features of the objects for correct perception, but also enables faster inference.

Committed to save computational cost of our proposed CFT model, we further present a lightweight view-aware attention (VA) instead of geometry-guided sparse sampling, simultaneously applied to the intra- and inter-view transformation. In addition to effectively reducing FLOPs and memory, view-attention ignores redundant computations, which promotes faster learning of attention. Compared with global attention, our built different schemes of view selection on BEV all achieve better results.

Overall, our contributions could be summarized as follows:

- We propose CFT to learn robust BEV representation for multi-camera 3D object detection without camera parameters. It is the first work that achieves comparable or even superior performance than geometry-dependent methods in terms of accuracy and speed (45.5% NDS, 3.6 FPS vs 44.8% NDS, 2.7 FPS).
- We design PA in obtaining richer 3D information of BEV, which could fully mine height features from content embedding, promoting the establishment of relationships between image views and BEV.
- VA is presented for reducing redundant computation. In comparison with global transformation, the FLOPs of the attention and the memory is reduced by about 60% ~ 78% and 12% ~ 17% in VA. Additionally, it promotes better interaction within the effective region.
- Experiments on nuScenes detection task evaluate that our proposed CFT achieves 49.7% NDS (Oct. 5th, 2022), competitive compared to the state-of-the-art methods without temporal or other modal input (50.4% NDS) on the leaderboard. In particular, CFT has no degradation compared to other models for noisy extrinsics.

2 Related work

Multi-camera 3D object detection predicts the 3D bounding boxes of the objects of interest from the input surrounding views. Motivated by typical works in 2D detection [6, 55, 38], researchers combine 3D prior and propose different 3D object detection frameworks to directly achieve sparse object-level features extraction [45, 9, 37, 11]. In recent new paradigms of autonomous driving, the BEV space attracts much attention because of its advantages in perception [35, 47, 56, 7, 33], prediction [1, 14], multi-task learning [46, 51, 28, 5] and downstream planning [33], etc. Thus, some advanced methods perform 3D object detection with obtained representation on the BEV space. BEVDet and CenterPoint [48] perform keypoint-based detection [53] by locating the object center point on the map view. PETR and BEVFormer utilize the end-to-end 3D detection head in DETR [6], treating all BEV grids as dense queries. For detecting occluded and dynamic objects better, multi-frame temporal information is also introduced into the origin detection architecture [15, 26, 34].

Table 1: Comparison of related approaches. All of them are related to multi-camera 3D object detection or BEV representation learning. "✓" in camera-driven means that depth-based methods use camera parameters, while not further divided into explicit or implicit.

Method	Depth?	Camera-Driven?	BEV Representation?	Transformation Type?
BEVDet	✓	✓	✓	Point-wise
BEVDepth	✓	✓	✓	Point-wise
DETR3D	✗	Explicit	✗	Point-wise
PolarDETR	✗	Explicit	✗	Point-wise
BEVFormer	✗	Explicit	✓	Point-wise
GKT	✗	Explicit	✓	Point-wise
PETR	✗	Implicit	✓	Global
CVT	✗	Implicit	✓	Global
Ours	✗	✗	✓	View

To learn BEV representation from surrounding views, depth-based methods [33, 36, 21, 16, 43, 35] infer depth in image views and project them to the BEV plane with the extrinsics and intrinsics, where Unsupervised depth estimation remains challenges. Although BEVdepth [21] improves feature extracting and downstream tasks performance compared with other paradigms, additional supervision is a key issue, relatively more difficult to obtain. In contrast, inspired by the transformer framework for 2D object detection [55, 6], some works such as BEVformer [22, 17, 32, 8] emphasizes directly learning the transformation relationship between image view and BEV based on the attention mechanism. Specifically, they explicitly preset height or supervise the predicted height, then perform point-wise attention on BEV by sampling local image features according to the extrinsics and intrinsics. End-to-end representation learning and less computation are their advantages, but the reliance on 3D priors affects the robustness of the models, such as height errors or biases in camera parameters. Besides, coordinate transformation and sampling cause less efficient processing. Without the projection operation, PETR [25] and CVT [52] implicitly encodes the 3D information into image or BEV feature. But precise camera parameters are still necessary, which are indirectly used to guide the attention. Also, introducing global transformation increases the computational cost and optimization difficulty. Unlike previous methods, our proposed CFT does not estimate depth and completely removes camera parameters. Inspired by advanced vision transformers [29, 24, 20], CFT decouples the positional and content embedding in the position-aware enhancement, and further mines richer 3D information, thereby effectively learning stable BEV representations. Instead of point-wise attention with camera guidance or redundant global attention, a view-attention is presented to reduce the computational and accelerates the establishment of transformation relations.

For the various related approaches mentioned above, we summarize the main differences between some representative ones and our proposed CFT in the Tab. 1.

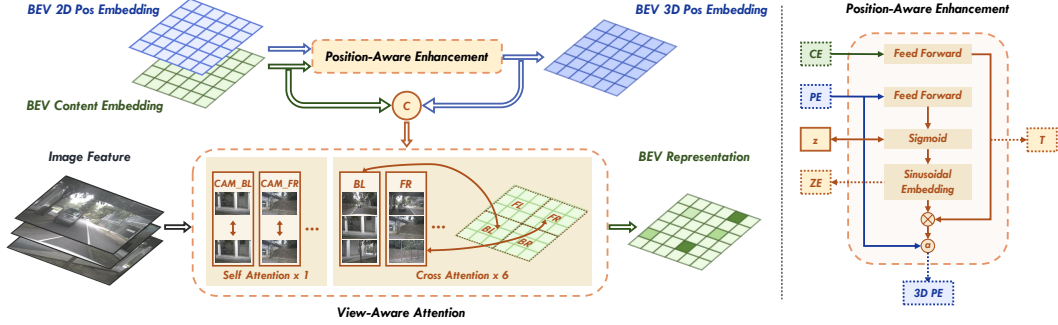


Figure 2: Our CFT for BEV representation learning. PA introduces separate content and 2D positional embedding for BEV feature, and the height embedding, ZE, is extracted from them, which is illustrated in the right part of the figure. With the encoding reorganization, (\otimes , \oplus , and \odot denotes dot, add, concatenation, respectively), the enhanced BEV feature is input to VA to interact with image features. Both self-attention and cross-attention are modulated in VA based on the view prior. Each view image in self-attention is computed only with itself, where CAM_BL , CAM_FR , etc. represent different surrounding views. In cross-attention, the BEV plane is divided to windows in various scheme, and BL , FR , etc. correspond to different parts. The image view groups are designed for each part to achieve more efficient calculation and accelerated convergence. After stacking multiple attention blocks, CFT completes the transformation of image views feature to BEV representation.

3 Method

3.1 Overall Architecture

In this work, we focus on attention-based 3D object detection without introducing temporal information and propose a entire architecture which thoroughly eliminates the influence of the camera parameters. We first begin with the multi-view images input, $I \in \mathbb{R}^{N_v \times H \times W \times 3}$, where N_v represents the number of views. Each view image is fed into a backbone network and neck layers for extracting multi-scale feature maps. In particular, we adopt the lowest scale feature map $F_s \in \mathbb{R}^{N_v \times H_s \times W_s \times C_s}$ for subsequent processing, i.e. only with the single-scale. Then F_s interacts with the BEV embedding for obtaining the BEV representation in our CFT, as shown in Fig. 2. CFT consists of two main parts: position-aware enhancement (PA) and view-aware attention (VA), which are utilized to capture BEV 3D positional information and perform lightweight attention, respectively. Finally, the prediction of the 3D bounding boxes is completed on the BEV space with the help of the designed detection head.

3.2 Position-Aware Enhancement

To capture 3D positional information in BEV without camera parameters, we start with common BEV 2D coordinates embedding $Q_p \in \mathbb{R}^{H_b \times W_b \times C_p}$ and further update it, which assigns a unique feature encoding to each BEV grid (h, w) . ‘ally, we first roughly infer the reference height z_{ref} for (h, w) on the basis of Q_p , and perform sinusoidal positional encoding [40] as follows:

$$Q_{ref} = \text{Sinusoidal}(z_{ref}), z_{ref} = \text{Norm}(\text{Sigmoid}(\text{FFN}(Q_p))), \quad (1)$$

where Norm scales the output of the activation layer to a preset height range, Q_{ref} means the reference height encoding. To adjust the height adaptively for different objects, we further introduce the BEV content embedding $Q_c \in \mathbb{R}^{H_b \times W_b \times C_s}$. Then the matrix M is learned based on Q_c for refining the object height, and obtaining the updated results. It can be described as

$$Q_{ep} = \text{add}(M \cdot Q_{ref}, Q_p), M = \text{FFN}(Q_c). \quad (2)$$

This operation could extract position-related information in the content, and obtain $Q_{ep} \in \mathbb{R}^{H_b \times W_b \times C_p}$, which enhances the original insufficient 2D coordinates embedding. The whole step is shown in Fig. 2. Considering that vanilla attention mixes the content and position, which is

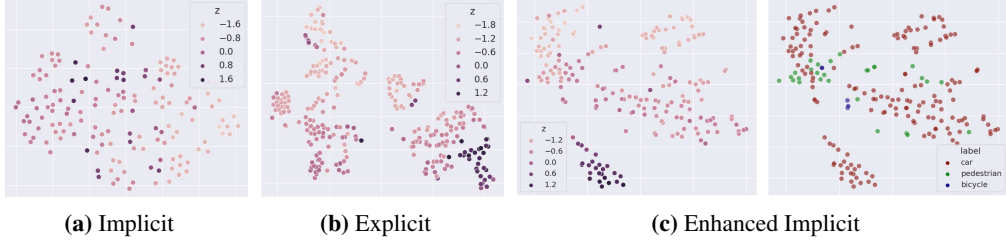


Figure 3: Relationship between z , labels and learned position embedding of objects. The visualization is implemented by t-sne, a common feature dimension reduction method. Scatters in the figure represent the feature of the BEV grids where the true objects are located. In the left of Fig. 3c, different colors denote the classes of objects corresponding to these features. In other figures, the shades of color correspond to their height variations. Fig. 3b and 3c show more separability in height relative to 3a, with a more continuous change in color. In particular, labels are marked in Fig. 3c as well, further demonstrating that rather than the category information, the height information are extracted from the content for refinement. In other words, on the same category, we can still learn corresponding embedding according to different heights.

not beneficial for our added Q_{ep} to correctly learn position information, we restructure the two parts both in images and BEV:

$$\begin{aligned} P_{image} &= \text{cat}(F_s, P_x, P_y, P_v), \\ P_{bev} &= \text{cat}(Q_c, Q_{ep}), \end{aligned} \quad (3)$$

where *cat* means the channel concatenation. The view encoding P_v indirectly takes into account the relative relationship of the cameras. P_{image} and P_{bev} are used to generate Q, K, V for attention. The above design clarifies the concept of content and position and ensures that position information is included in the refinement of the height. Even without introducing camera parameters, the sufficient interaction between Q_{ep} and P_x, P_y, P_z could guide the implicit learning of the coordinates mapping. In fact, the reference height z_{ref} in PA comes directly from Q_p , tending to learn the overall distribution of the data, so adaptive refinement helps to more accurately represent the true object height. Additionally, though PA adds supervision for learning z_{ref} with $L1$ loss by default, after removing the above supervision, the refined height embedding still exhibits the ability on height representation.

Fig. 3 demonstrates the feature visualization via t-sne [39], which compares the relationship between the refined height encoding and height ground truth under different designs. In details, Fig. 3a represents only using 2D positional information and vanilla attention to learn the transformation, Fig. 3b and 3c respectively indicate whether there is supervision for predicting z_{ref} in our PA. Regardless of the supervision, our PA helps the enhanced positional embedding of BEVs more correlated with height, whose height feature exhibits better separability compared to the simple design. Therefore, thanks to PA, camera extrinsics and intrinsics could be completely removed, still ensuring that 3D information is effectively learned.

3.3 View-Aware Attention

In standard global attention, P_{image} and P_{bev} will be flattened for calculation directly, excluding the channel dimension. Different from this computationally redundant method with high cost, our proposed view-level attention variant only considers valuable interactions, shown in Fig. 2. We first reshape the image encoding into $P'_{image} \in \mathbb{R}^{N_v \times H_s W_s \times C}$ to modulate self-attention, where $C = C_s + C_p$. Therefore, for each image, self-attention only involve $H_s W_s$ pixels in the same view. Then, we divide N_v windows along the spatial dimension on BEV encoding P_{bev} . In fact, there are multiple division methods, bringing different benefits in terms of computation reduction and performance improvement. We choose the strategy with the best balance, which will be further analyzed theoretically and experimentally in Sec. 4.4.

Taking a rectangular division as an example, our method reshape P_{bev} into $P'_{bev} \in \mathbb{R}^{N_v \times \frac{H_b}{N_H} \cdot \frac{W_b}{N_W} \times C}$, where $N_v = N_H N_W, N_H = 2, N_W = 2$. It covers four BEV windows, FL, FR, BL , and BR in Fig. 2. To preserve effective information, instead of performing cross-attention calculation on P'_{image} and P'_{bev} , we continue to divide the view groups $G \in \mathbb{R}^{N_v \times N_g H_s W_s \times C}$ from P'_{image} . Points from different windows on the BEV feature will interact with different view groups. The specific division is as follows:

$$\begin{aligned} G_{FL} &= \text{cat}(P'_{CAM_FL}, P'_{CAM_F}, P'_{CAM_BL}), & G_{FR} &= \text{cat}(P'_{CAM_F}, P'_{CAM_FR}, P'_{CAM_BR}), \\ G_{BL} &= \text{cat}(P'_{CAM_FL}, P'_{CAM_BL}, P'_{CAM_B}), & G_{BR} &= \text{cat}(P'_{CAM_FR}, P'_{CAM_B}, P'_{CAM_BR}), \end{aligned} \quad (4)$$

where different P' correspond to six views front-left, front, front-right, back-left, back, back-right respectively. Accordingly, for the grids of BL window in P'_{bev} , we choose view group G_{BL} to contribute keys, where the content part contributes values for cross-attention, other windows perform similar calculations. After multiple layers of cross-attention, we obtain the final BEV representation $F_B \in \mathbb{R}^{H_b \times W_b \times C_s}$.

Our attention variant introduces view priors without relying on the extrinsics and intrinsics. In addition to reducing memory cost, it also removes redundant information via roughly considering the camera range, which is beneficial to learn BEV feature faster and better. VA is inherently robust to camera parameters and leads to more efficient inference than geometry-guided attention.

3.4 Detection Head

We upsampled the BEV expression F_B by a factor of 4 to obtain a large resolution BEV feature map $F'_B \in \mathbb{R}^{4H_b \times 4W_b \times C_s}$, which is beneficial for small object detection. For 3D object detection task on F'_B , we adopt the single-stage CenterPoint [48] as detection head to predict the center heatmap with focal loss and regression map with $L1$ loss. Additionally, we make several adjustments to further simplify the training pipeline. We remove the structure of separate heads for different classes and regression terms, and set all Gaussian kernels to a fixed size when generating the ground truth. During inference, we utilize scale-nms [16] for decoding and post-processing of bounding boxes.

4 Experiment

4.1 Datasets and evaluation metrics

We conduct all the experiments on the nuScenes [4], a public large-scale autonomous driving dataset. The nuScenes dataset collects 1000 driving scenes with 20 second length and manually divides the training set, validation set and test set. Our results are all from the evaluation of the *val* set or the *test* set. We mainly use 6-views images with size 1600×900 and annotations of 3D bounding boxes provided in 40k keyframes. For the detection task, these annotations come from 10 categories with their respective detection ranges.

We evaluate our approaches according to the official evaluation metrics provided by nuScenes, including mean Average Precision (mAP), a set of true positive metrics that measure translation (ATE), scale (ASE), orientation (AOE), velocity (AVE) and attribute (AAE) errors. Finally, the comprehensive score, nuScenes detection score (NDS), is derived from the weighted sum of the above metrics:

$$NDS = \frac{1}{10} \left[5mAP + \sum_{mTP} \max(1 - mTP, 0) \right]. \quad (5)$$

4.2 Implementation details

We adopt ResNet-101 [13] backbone, pretrained by FCOS3D [44], and FPN [23] neck to extract image feature for our CFT by default, where image size is 1600×640 . For the outputs of ResNet, we choose the feature map of size $1/64$ and dimension $C_s = 256$. We set BEV content and positional embedding as $64 \times 64 \times 256$, corresponding to the perception ranges of $[-51.2m, 51.2m]$ for the

X and Y axis. In VA module, they are divided into 4 windows with the size of 32×32 , and fed into 1 layer of self-attention and 6 layers of cross-attention. In the default detection head, we set the heatmap of each object to 9×9 Gaussian kernel to generate ground truth. During bounding boxes decoding, scale-nms is consistent with BEVDet.

Except the model for official testing is trained on 8 Tesla V100, others are run on 8 RTX3090 GPUs, with 24 epochs and a total batch size of 8. We choose the AdamW [27] optimizer with a step learning rate policy, which drops the learning rate at 20 and 23 epoch by a factor of 0.1. Learning rate is set to 2×10^{-4} .

Table 2: Comparison with state-of-the-art methods on nuScenes *val* set. BEVDepth-S is BEVDepth with # is trained with CBGS [54]. † means that the multi-scale feature maps are utilized. For the fair comparison of the inference speed, FPS is evaluated under two different devices, 1 RTX3090 and 1 Tesla V100, which are abbreviated as G and T to ensure the alignment of different methods.

Method	Size	NDS \uparrow	mAP \uparrow	mATE \downarrow	mASE \downarrow	mAOE \downarrow	mAVE \downarrow	mAAE \downarrow	FPS \uparrow
DETR3D \dagger	1600 \times 900	0.425	0.346	0.773	0.268	0.383	0.842	0.216	2.0 (G)
BEVFormer \dagger	1600 \times 900	0.448	0.375	0.725	0.272	0.391	0.802	0.216	2.7 (G)
BEVDepth-S	1408 \times 512	0.408	0.376	0.659	0.267	0.543	1.059	0.335	5.2 (G)
CFT-BEV3D	1600 \times 900	<u>0.445</u>	0.335	0.716	0.277	0.373	0.671	0.187	3.6 (G)
CFT-BEV3D	1600 \times 640	0.444	0.334	0.715	0.278	0.374	0.689	0.177	5.0 (G)
CFT-BEV3D	1408 \times 512	0.415	0.307	0.732	0.276	0.476	0.713	0.186	6.0 (G)
DETR3D $\#\dagger$	1600 \times 900	0.434	0.349	0.716	0.268	0.379	0.842	0.200	X
PETR $\#$	1600 \times 900	0.442	0.370	0.711	0.267	0.412	0.834	0.190	1.7 (T)
CFT-BEV3D $\#$	1600 \times 900	0.455	0.343	0.651	0.274	0.338	0.716	0.184	2.6 (T)

Table 3: Comparison with state-of-the-art methods on nuScenes *test* set. The underline indicates that our CFT-BEV3D achieves the second best performance (until 05 October, 2022).

Method	Multi-Scale	NDS \uparrow	mAP \uparrow	mATE \downarrow	mASE \downarrow	mAOE \downarrow	mAVE \downarrow	mAAE \downarrow
DETR3D	✓	0.479	0.412	0.641	0.255	0.394	0.845	0.133
BEVFormer	✓	0.495	0.435	0.589	0.254	0.402	0.842	0.131
PETR		0.504	0.441	0.593	0.249	0.383	0.808	0.132
BEVDet		0.488	0.424	0.524	0.242	0.373	0.950	0.148
CFT-BEV3D		<u>0.497</u>	0.416	0.518	0.250	0.390	0.829	0.124

4.3 Main Results

4.3.1 nuScenes *val* set

We compare the proposed method with four state-of-the-art models, DETR3D, BEVFormer, BEVDepth and PETR, as shown in Tab. 2, where CFT-BEV3D represents our CFT model for the 3D object detection task. For a fair comparison, we input image views with different sizes to align other methods. Under the same conditions, CFT-BEV3D outperforms DETR3D and PETR by 2.1% (or 2.0% without CBGS) and 1.3% on NDS, respectively. At a smaller size of 1600×640 , CFT-BEV3D still exceeds DETR3D 1.9%. In particular, even if we do not use the multi-scale feature, we can still obtain a competitive NDS score (-0.3% vs BEVFormer) compared to the multi-scale methods. Compared to the advanced method with additional deep supervision, BEVDepth, our method is still 0.7% NDS higher at the same resolution 1408×512 . Notably, even though BEVdepth surpasses most methods with larger resolution on mAP and mATE due to its accurate depth estimation, other metrics is relative low, so inferior to our CFT-BEV3D. In terms of inference speed, CFT-BEV3D exhibits higher FPS across different input scales. Furthermore, unlike other methods whose performance degrades under noisy extrinsics, CFT-BEV3D is stable, which could be far superior to other methods. Noise analysis of camera parameters will be more discussed in Sec. 4.4.3.

4.3.2 nuScenes test set

Tab. 3 shows a comparison of methods without temporal input and other modal information on the nuScenes detection task leaderboard. All the models are trained with VoVNetV2 [19] backbone, pretrained by DD3D [31]. The difference is that our CFT-BEV3D exploits a smaller (1600×640) resolution input and obtains the comparable NDS score, which is the second best and 0.7% lower than PETR.

Table 4: Different embedding design. "Implicit" means a naive design with 2D learned positional embedding for image views and BEV, and the embedding is mixed for vanilla global attention. "Explicit" and "Enhanced Implicit" means whether if there is explicit supervision of reference height in our PA.

Method	NDS \uparrow	mAP \uparrow	mATE \downarrow	mASE \downarrow	mAOE \downarrow
Implicit	0.424	0.320	0.709	0.278	0.419
Explicit	0.444	0.334	0.715	0.278	0.374
Enhanced Implicit	0.440	0.340	0.700	0.281	0.409

Overall, all the experiments illustrate that our CFT has a good performance on 3D object detection, comparable to some state-of-the-art methods. It maintains robustness to camera parameter with different noise levels, and achieves a balance of speed and performance.

4.4 Ablation studies

In this section, we follow the configuration without CBGS training and on the nuscene validation set. To emphasize the importance of obtaining a model robust to camera parameters, we additionally perform noisy extrinsics analysis, mainly involving PETR and BEVFormer that outperform our CFT-BEV3D in Sec. 4.3.

4.4.1 Embedding Designs

When constructing embedding based on our designed PA to enhance position information, we conduct experiments with three strategies for comparison: implicit, explicit and enhanced implicit, mentioned in Sec.3. The detailed explanations and results are shown in Tab. 4.

Compared with the learned embedding, our "Explicit" PA improves 2.0% on NDS, in which the improvement of mAOE and mAP is obvious by 4.5% and 1.4%. It shows that the additional 3D enhanced information helps each BEV grid better correspond to the true position, which is beneficial to capture the correct image features. They are presented in the map view, thereby improving the prediction of orientation and category. Specially, "Enhanced Implicit" PA is comparable to "Explicit" on NDS, only the mAOE is slightly worse.

The above experiments demonstrate that thanks to the design of PA, 3D information can be properly learned and enhanced to guide better feature transformation from image views to BEV.

4.4.2 BEV Window Division

To perform cross-attention in VA, BEV needs to be divided into multiple windows, and various partitioning methods could be considered. For choosing the optimal partitioning method as possible to balance the performance and computational cost, we have fully experimented with 4 different strategies in Fig. 4. Before comparing the results experimentally, we first conduct a theoretical analysis of these strategies, calculating the computational reduction they bring compared to global attention:

$$\begin{aligned}
 C_g &= O(6H_s W_s H_b W_b C) &= O(24576H_s W_s C) \\
 C_a &= O(4 \cdot 3H_s W_s \cdot \frac{H_b}{2} \cdot \frac{W_b}{2} \cdot C) &= O(12288H_s W_s C)
 \end{aligned}$$

$$\begin{aligned}
C_b &= O(6 \cdot 3H_s W_s \cdot \frac{H_b}{2} \cdot \lceil \frac{W_b}{3} \rceil \cdot C) = O(12672H_s W_s C) \\
C_c &\approx O(6 \cdot H_s W_s \cdot \lceil S \rceil \cdot C) = O(4374H_s W_s C) \\
C_d &\approx O(6 \cdot 2H_s W_s \cdot \lceil S \rceil \cdot C) = O(8748H_s W_s C),
\end{aligned}$$

Table 5: Different attention types. Global means vanilla multi-head attention. At an input resolution of 1600×900 , only the experiments with global attention or (a) are performed, which is the chosen method according to the smaller resolution. \times means that the cost of global attention at a large resolution is too high and exceeds the memory limit.

Size	Global	Rec 2×2	Rec 2×3	Polar A	Polar B	NDS \uparrow	FLOPs \downarrow	Memory \downarrow
1600×640	✓					0.434	69.2G	19.0G
		✓				0.444	27.4G	16.8G
			✓			0.432	25.5G	17.0G
				✓		0.431	14.9G	15.8G
					✓	0.439	20.6G	16.4G
1600×900	✓					\times	87.7G	\times
		✓				0.455	35.8G	23.0G

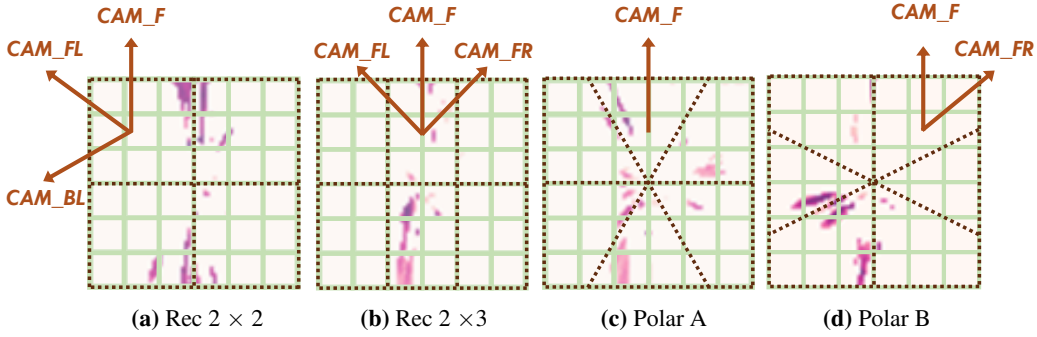


Figure 4: BEV Window Division. The four window divisions are accomplished on BEV feature. Instead of listing each view group G in detail, only the calculation of one window is given in the figure. Among them, (a) and (b) are rectangular divisions, and each window is interacted with three image views. (c) and (d) treats the BEV plane as in the polar coordinate system and divides it, whose G includes one or two image views, respectively. For some methods, the number of grids in different windows is not equal, so we perform the zero padding additionally for batch operation.

where $H_b = W_b = 64$ and $S = \frac{1}{2} \cdot \frac{H_b}{2} \left[W_b - \frac{H_b}{2\sqrt{3}} \right]$, the area of the largest divided part. It can be seen that (c) and (d) could contribute lower computational cost among all the methods, but in fact, they are more complicated and depend on the prior of the view, different from the rectangular windows. (a) and (b) have similar effects and reduce the computation by nearly half compared to the vanilla multi-head attention.

The experimental results are given in Fig. 5, which contains the comparison of two input image sizes under different attention types in terms of detection scores, computation, memory. For 1600×640 input, improvements of memory and FLOPs are basically consistent with the theoretical analysis, where (a) is slightly worse than (b) in Flops because it consider the calculation of the whole transformer. Although (c) performs the best on computational cost reduction, the NDS score is lower than other methods (-1.3% vs (a)) due to its insufficient representation learning, only using one view. In contrast, (a) and (d) both achieve a good balance, whose NDS is better than global attention by about 1.0% and 0.5% , along with sufficient cost reduction. Especially, all of our attention variants could achieve the comparable or better performance than origin attention in detection, demonstrating that VA effectively discards the redundant feature, promotes interactions within the effective region, and even improves the ability to learn BEV representation.

Focusing on detection performance, we finally choose the partitioning method of (a) and conduct the experiment with larger resolution 1600×900 , which shows that the computational cost optimization is sufficient compared to global attention.

In summary, VA, as our proposed novel attention variant, improves the original global attention cost and also replaces the unstable geometry-guidance attention. It is robust to camera parameters variation, ensuring sufficient receptive field and realizing the stable learning of potential view transformation.

4.4.3 Noisy Extrinsic Analysis

To analyze the impact of camera parameters on BEV representation learning, we adopt the extrinsic noises in [22]. It is applied on PETR, BEVFormer and our CFT-BEV3D to evaluate the trained model as shown in the results in Fig. 5. Under the accurate extrinsics, the NDS score of CFT-BEV3D is slightly lower compared with other models of the same configuration. However, it is naturally undisturbed by the noise level variation with stable results. Even with a small perturbation of the parameters, BEVformer drops by 0.6% – 6.8% NDS and PETR drops by 4.7% – 7.6%, but our method is not vulnerable to these perturbations and shows an evident improvement. The above degradation issues and results caused by the unstable camera parameters illustrate the importance of calibration free model, and confirms that competitive results can be obtained without relying on parameters guidance, whose stable performance is also more contributing to further expansion and application.

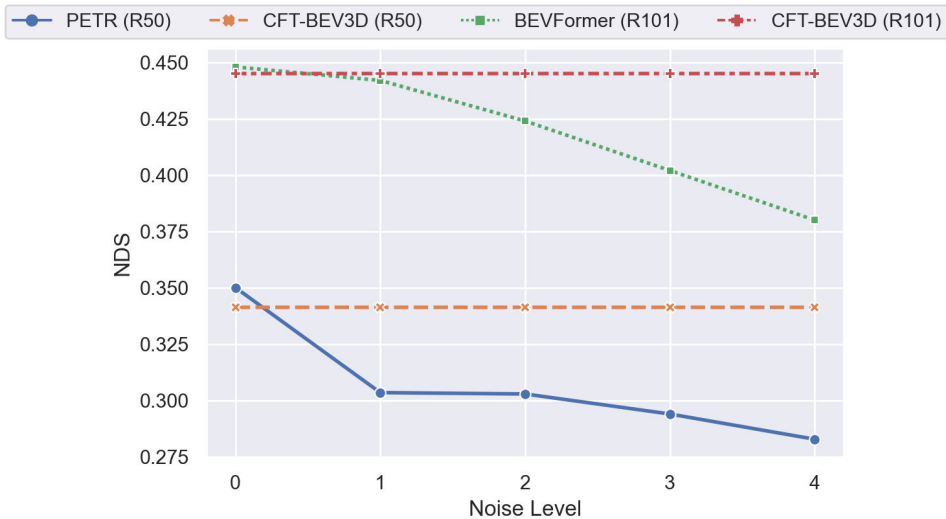


Figure 5: The performance of different models under noisy extrinsics. The implementation of the noises is the same as [22]. The PETR (R50) is evaluated on the official pre-trained model, and our CFT-BEV3D (R50) is trained with the aligned common configuration.

4.5 Visualization

For the qualitative results, we show the visualization of detection results in Sec. A.1 and attention in Fig. 6. Specifically, we select the center points of objects with high confidence in the BEV plane, and visualize the bounding boxes predicted based on them. Then for a specific box, as the sample circled on the *LIDAR_TOP*, we can visual the attention map calculated on each view in the corresponding view group. Three examples in Fig. 6 show the results with different view groups. To further clarify the implicit enhancement of 3D information by PA, we choose the enhanced implicit design for the embedding. In fact, our model exhibits high responses to object regions, and are generally unresponsive in views without objects as shown in our samples. Also, VA effectively preserves the information, accelerates the convergence, and learns the transformation between image views and BEV without any geometry guidance.

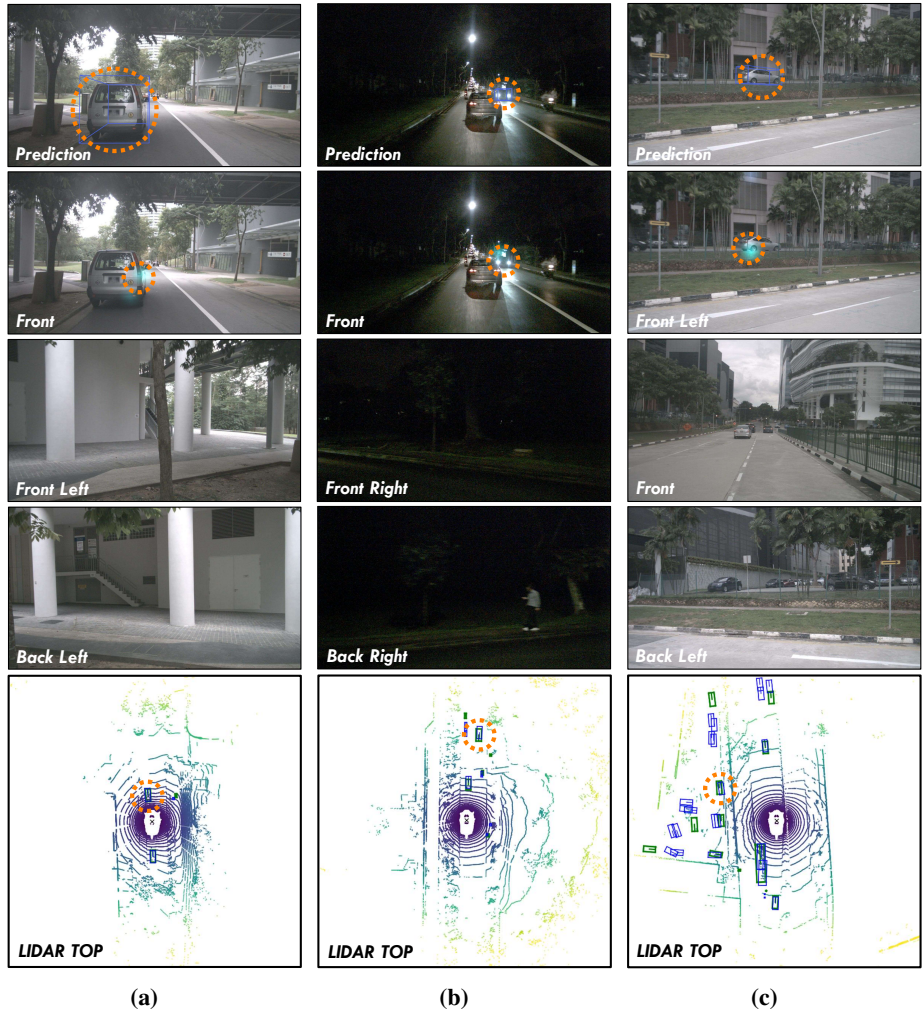


Figure 6: The attention weight maps of three views in the view group. Each column shows a sample, in which the first row shows the object for visualization and its detection results. Three objects are located in the FL, FR, and FL window of the BEV, respectively.

5 Conclusions

In this paper, we present an approach for learning BEV representation from image views via a completely camera calibration free view transformation. Our proposed CFT is the first parameters-free work, comparable to the state-of-the-art methods in 3D object detection, thanks to learning mapping implicitly with enhanced 3D information. Moreover, we propose an attention variant, which enables the model to reduce memory, computation cost and converge better. Unlike existing CFT is naturally robust to camera parameters noise. In the near future, we will explore combining CFT with temporal or additional modalities.

References

- [1] Adil Kaan Akan and Fatma Guney. Stretchbev: Stretching future instance prediction spatially and temporally. *European Conference on Computer Vision (ECCV)*, 2022. 3
- [2] Xuyang Bai, Zeyu Hu, Xinge Zhu, Qingqiu Huang, Yilun Chen, Hongbo Fu, and Chiew-Lan Tai. Transfusion: Robust lidar-camera fusion for 3d object detection with transformers. In *Proceedings of the IEEE/CVF Conference on Computer Vision and Pattern Recognition*, pages 1090–1099, 2022. 1

- [3] Alex Bewley, Pei Sun, Thomas Mensink, Dragomir Anguelov, and Cristian Sminchisescu. Range conditioned dilated convolutions for scale invariant 3d object detection. *arXiv preprint arXiv:2005.09927*, 2020. 1
- [4] Holger Caesar, Varun Bankiti, Alex H. Lang, Sourabh Vora, Venice Erin Liong, Qiang Xu, Anush Krishnan, Yu Pan, Giancarlo Baldan, and Oscar Beijbom. nuscenes: A multimodal dataset for autonomous driving. *arXiv preprint arXiv:1903.11027*, 2019. 6
- [5] Yigit Baran Can, Alexander Liniger, Danda Pani Paudel, and Luc Van Gool. Structured bird’s-eye-view traffic scene understanding from onboard images. In *Proceedings of the IEEE/CVF International Conference on Computer Vision*, pages 15661–15670, 2021. 3
- [6] Nicolas Carion, Francisco Massa, Gabriel Synnaeve, Nicolas Usunier, Alexander Kirillov, and Sergey Zagoruyko. End-to-end object detection with transformers. In *European conference on computer vision*, pages 213–229. Springer, 2020. 3
- [7] Li Chen, Chonghao Sima, Yang Li, Zehan Zheng, Jiajie Xu, Xiangwei Geng, Hongyang Li, Conghui He, Jianping Shi, Yu Qiao, et al. Persformer: 3d lane detection via perspective transformer and the openlane benchmark. *arXiv preprint arXiv:2203.11089*, 2022. 3
- [8] Shaoyu Chen, Tianheng Cheng, Xinggang Wang, Wenming Meng, Qian Zhang, and Wenyu Liu. Efficient and robust 2d-to-bev representation learning via geometry-guided kernel transformer. *arXiv preprint arXiv:2206.04584*, 2022. 3
- [9] Shaoyu Chen, Xinggang Wang, Tianheng Cheng, Qian Zhang, Chang Huang, and Wenyu Liu. Polar parametrization for vision-based surround-view 3d detection. *arXiv preprint arXiv:2206.10965*, 2022. 1, 3
- [10] Xiaozhi Chen, Huimin Ma, Ji Wan, Bo Li, and Tian Xia. Multi-view 3d object detection network for autonomous driving. In *Proceedings of the IEEE conference on Computer Vision and Pattern Recognition*, pages 1907–1915, 2017. 1
- [11] Zehui Chen, Zhenyu Li, Shiquan Zhang, Liangji Fang, Qinhong Jiang, and Feng Zhao. Graphdetr3d: Rethinking overlapping regions for multi-view 3d object detection. *arXiv preprint arXiv:2204.11582*, 2022. 3
- [12] Zehui Chen, Zhenyu Li, Shiquan Zhang, Liangji Fang, Qinhong Jiang, Feng Zhao, Bolei Zhou, and Hang Zhao. Autoalign: Pixel-instance feature aggregation for multi-modal 3d object detection. In *Proceedings of the Thirty-First International Joint Conference on Artificial Intelligence, IJCAI-22*, pages 827–833, 7 2022. 1
- [13] Kaiming He, Xiangyu Zhang, Shaoqing Ren, and Jian Sun. Deep residual learning for image recognition. In *Proceedings of the IEEE conference on computer vision and pattern recognition*, pages 770–778, 2016. 6
- [14] Anthony Hu, Zak Murez, Nikhil Mohan, Sofia Dudas, Jeffrey Hawke, Vijay Badrinarayanan, Roberto Cipolla, and Alex Kendall. Fiery: Future instance prediction in bird’s-eye view from surround monocular cameras. In *Proceedings of the IEEE/CVF International Conference on Computer Vision*, pages 15273–15282, 2021. 3
- [15] Junjie Huang and Guan Huang. Bevdet4d: Exploit temporal cues in multi-camera 3d object detection. *arXiv preprint arXiv:2203.17054*, 2022. 3
- [16] Junjie Huang, Guan Huang, Zheng Zhu, and Dalong Du. Bevdet: High-performance multi-camera 3d object detection in bird-eye-view. *ArXiv*, abs/2112.11790, 2021. 1, 3, 6
- [17] Yanqin Jiang, Li Zhang, Zhenwei Miao, Xiatian Zhu, Jin Gao, Weiming Hu, and Yu-Gang Jiang. Polarformer: Multi-camera 3d object detection with polar transformers. *arXiv preprint arXiv:2206.15398*, 2022. 1, 3
- [18] Alex H Lang, Sourabh Vora, Holger Caesar, Lubing Zhou, Jiong Yang, and Oscar Beijbom. Pointpillars: Fast encoders for object detection from point clouds. In *Proceedings of the IEEE/CVF conference on computer vision and pattern recognition*, pages 12697–12705, 2019. 1
- [19] Youngwan Lee and Jongyoul Park. Centermask: Real-time anchor-free instance segmentation. In *Proceedings of the IEEE/CVF conference on computer vision and pattern recognition*, pages 13906–13915, 2020. 8

- [20] Feng Li, Hao Zhang, Shilong Liu, Jian Guo, Lionel M Ni, and Lei Zhang. Dn-detr: Accelerate detr training by introducing query denoising. In *Proceedings of the IEEE/CVF Conference on Computer Vision and Pattern Recognition*, pages 13619–13627, 2022. 3
- [21] Yin hao Li, Zheng Ge, Guanyi Yu, Jinrong Yang, Zengran Wang, Yukang Shi, Jianjian Sun, and Zeming Li. Bevdepth: Acquisition of reliable depth for multi-view 3d object detection. *arXiv preprint arXiv:2206.10092*, 2022. 1, 3
- [22] Zhiqi Li, Wenhai Wang, Hongyang Li, Enze Xie, Chonghao Sima, Tong Lu, Qiao Yu, and Jifeng Dai. Bevformer: Learning bird’s-eye-view representation from multi-camera images via spatiotemporal transformers. *ArXiv*, abs/2203.17270, 2022. 1, 2, 3, 10
- [23] Tsung-Yi Lin, Piotr Dollár, Ross Girshick, Kaiming He, Bharath Hariharan, and Serge Belongie. Feature pyramid networks for object detection. In *Proceedings of the IEEE conference on computer vision and pattern recognition*, pages 2117–2125, 2017. 6
- [24] Shilong Liu, Feng Li, Hao Zhang, Xiao Yang, Xianbiao Qi, Hang Su, Jun Zhu, and Lei Zhang. DAB-DETR: Dynamic anchor boxes are better queries for DETR. In *International Conference on Learning Representations*, 2022. 3
- [25] Ying-Hao Liu, Tiancai Wang, X. Zhang, and Jian Sun. Petr: Position embedding transformation for multi-view 3d object detection. *ArXiv*, abs/2203.05625, 2022. 1, 3
- [26] Yingfei Liu, Junjie Yan, Fan Jia, Shuailin Li, Qi Gao, Tiancai Wang, Xiangyu Zhang, and Jian Sun. PetrV2: A unified framework for 3d perception from multi-camera images. *arXiv preprint arXiv:2206.01256*, 2022. 1, 2, 3
- [27] Ilya Loshchilov and Frank Hutter. Decoupled weight decay regularization. In *International Conference on Learning Representations*, 2019. 7
- [28] Jiachen Lu, Zheyuan Zhou, Xiatian Zhu, Hang Xu, and Li Zhang. Learning ego 3d representation as ray tracing. *arXiv preprint arXiv:2206.04042*, 2022. 3
- [29] Depu Meng, Xiaokang Chen, Zejia Fan, Gang Zeng, Houqiang Li, Yuhui Yuan, Lei Sun, and Jingdong Wang. Conditional detr for fast training convergence. In *Proceedings of the IEEE International Conference on Computer Vision (ICCV)*, 2021. 3
- [30] Ramin Nabati and Hairong Qi. Centerfusion: Center-based radar and camera fusion for 3d object detection. In *Proceedings of the IEEE/CVF Winter Conference on Applications of Computer Vision*, pages 1527–1536, 2021. 1
- [31] Dennis Park, Rares Ambrus, Vitor Guizilini, Jie Li, and Adrien Gaidon. Is pseudo-lidar needed for monocular 3d object detection? In *Proceedings of the IEEE/CVF International Conference on Computer Vision*, pages 3142–3152, 2021. 8
- [32] Lang Peng, Zhirong Chen, Zhangjie Fu, Pengpeng Liang, and Erkang Cheng. Bevsegformer: Bird’s eye view semantic segmentation from arbitrary camera rigs. *arXiv preprint arXiv:2203.04050*, 2022. 3
- [33] Jonah Philion and Sanja Fidler. Lift, splat, shoot: Encoding images from arbitrary camera rigs by implicitly unprojecting to 3d. In *Proceedings of the European Conference on Computer Vision*, 2020. 2, 3
- [34] Zequn Qin, Jingyu Chen, Chao Chen, Xiaozhi Chen, and Xi Li. Uniformer: Unified multi-view fusion transformer for spatial-temporal representation in bird’s-eye-view. *arXiv preprint arXiv:2207.08536*, 2022. 3
- [35] Cody Reading, Ali Harakeh, Julia Chae, and Steven L Waslander. Categorical depth distribution network for monocular 3d object detection. In *Proceedings of the IEEE/CVF Conference on Computer Vision and Pattern Recognition*, pages 8555–8564, 2021. 3
- [36] Danila Rukhovich, Anna Vorontsova, and Anton Konushin. Imvoxelnet: Image to voxels projection for monocular and multi-view general-purpose 3d object detection. In *Proceedings of the IEEE/CVF Winter Conference on Applications of Computer Vision*, pages 2397–2406, 2022. 3
- [37] Yining Shi, Jingyan Shen, Yifan Sun, Yunlong Wang, Jiabin Li, Shiqi Sun, Kun Jiang, and Diange Yang. Srcn3d: Sparse r-cnn 3d surround-view camera object detection and tracking for autonomous driving. *arXiv preprint arXiv:2206.14451*, 2022. 1, 3

- [38] Peize Sun, Rufeng Zhang, Yi Jiang, Tao Kong, Chenfeng Xu, Wei Zhan, Masayoshi Tomizuka, Lei Li, Zehuan Yuan, Changhu Wang, et al. Sparse r-cnn: End-to-end object detection with learnable proposals. In *Proceedings of the IEEE/CVF conference on computer vision and pattern recognition*, pages 14454–14463, 2021. 3
- [39] Laurens van der Maaten and Geoffrey Hinton. Visualizing data using t-sne. *Journal of Machine Learning Research*, 9(86):2579–2605, 2008. 5
- [40] Ashish Vaswani, Noam Shazeer, Niki Parmar, Jakob Uszkoreit, Llion Jones, Aidan N Gomez, Łukasz Kaiser, and Illia Polosukhin. Attention is all you need. *Advances in neural information processing systems*, 30, 2017. 1, 4
- [41] Sourabh Vora, Alex H Lang, Bassam Helou, and Oscar Beijbom. Pointpainting: Sequential fusion for 3d object detection. In *Proceedings of the IEEE/CVF conference on computer vision and pattern recognition*, pages 4604–4612, 2020. 1
- [42] Chunwei Wang, Chao Ma, Ming Zhu, and Xiaokang Yang. Pointaugmenting: Cross-modal augmentation for 3d object detection. In *Proceedings of the IEEE/CVF Conference on Computer Vision and Pattern Recognition (CVPR)*, pages 11794–11803, June 2021. 1
- [43] Tai Wang, Qing Lian, Chenming Zhu, Xinge Zhu, and Wenwei Zhang. Mv-fcos3d++: Multi-view camera-only 4d object detection with pretrained monocular backbones. *arXiv preprint arXiv:2207.12716*, 2022. 3
- [44] Tai Wang, Xinge Zhu, Jiangmiao Pang, and Dahua Lin. Fcos3d: Fully convolutional one-stage monocular 3d object detection. In *Proceedings of the IEEE/CVF International Conference on Computer Vision*, pages 913–922, 2021. 6
- [45] Yue Wang, Vitor Campanholo Guizilini, Tianyuan Zhang, Yilun Wang, Hang Zhao, and Justin Solomon. Detr3d: 3d object detection from multi-view images via 3d-to-2d queries. In *CoRL*, 2021. 1, 3
- [46] Enze Xie, Zhiding Yu, Daquan Zhou, Jonah Philion, Anima Anandkumar, Sanja Fidler, Ping Luo, and Jose M Alvarez. M²2bev: Multi-camera joint 3d detection and segmentation with unified birds-eye view representation. *arXiv preprint arXiv:2204.05088*, 2022. 3
- [47] Weixiang Yang, Qi Li, Wenxi Liu, Yuanlong Yu, Yuexin Ma, Shengfeng He, and Jia Pan. Projecting your view attentively: Monocular road scene layout estimation via cross-view transformation. In *Proceedings of the IEEE/CVF Conference on Computer Vision and Pattern Recognition*, pages 15536–15545, 2021. 3
- [48] Tianwei Yin, Xingyi Zhou, and Philipp Krähenbühl. Center-based 3d object detection and tracking. *CVPR*, 2021. 3, 6
- [49] Tianwei Yin, Xingyi Zhou, and Philipp Krähenbühl. Multimodal virtual point 3d detection. *Advances in Neural Information Processing Systems*, 34:16494–16507, 2021. 1
- [50] Jin Hyeok Yoo, Yecheol Kim, Jisong Kim, and Jun Won Choi. 3d-cvf: Generating joint camera and lidar features using cross-view spatial feature fusion for 3d object detection. In *European Conference on Computer Vision*, pages 720–736. Springer, 2020. 1
- [51] Yunpeng Zhang, Zheng Zhu, Wenzhao Zheng, Junjie Huang, Guan Huang, Jie Zhou, and Jiwen Lu. Beverse: Unified perception and prediction in birds-eye-view for vision-centric autonomous driving. *arXiv preprint arXiv:2205.09743*, 2022. 1, 3
- [52] Brady Zhou and Philipp Krähenbühl. Cross-view transformers for real-time map-view semantic segmentation. In *Proceedings of the IEEE/CVF Conference on Computer Vision and Pattern Recognition (CVPR)*, pages 13760–13769, June 2022. 1, 3
- [53] Xingyi Zhou, Dequan Wang, and Philipp Krähenbühl. Objects as points. *arXiv preprint arXiv:1904.07850*, 2019. 3
- [54] Benjin Zhu, Zhengkai Jiang, Xiangxin Zhou, Zeming Li, and Gang Yu. Class-balanced grouping and sampling for point cloud 3d object detection. *arXiv preprint arXiv:1908.09492*, 2019. 7
- [55] Xizhou Zhu, Weijie Su, Lewei Lu, Bin Li, Xiaogang Wang, and Jifeng Dai. Deformable detr: Deformable transformers for end-to-end object detection. *arXiv preprint arXiv:2010.04159*, 2020. 3
- [56] Jiayu Zou, Junrui Xiao, Zheng Zhu, Junjie Huang, Guan Huang, Dalong Du, and Xingang Wang. Hft: Lifting perspective representations via hybrid feature transformation. *arXiv preprint arXiv:2204.05068*, 2022. 3

A Appendix

A.1 Visualizations

We visualize our 3D object detection results in Fig. 7. The prediction results in BEV are close to the ground truth, indicating that our method performs well within the effective detection range. Since the BEV size we directly utilize for cross-attention is only 64, which may be unfavorable for detection of some objects with small 2D size such as pedestrians.

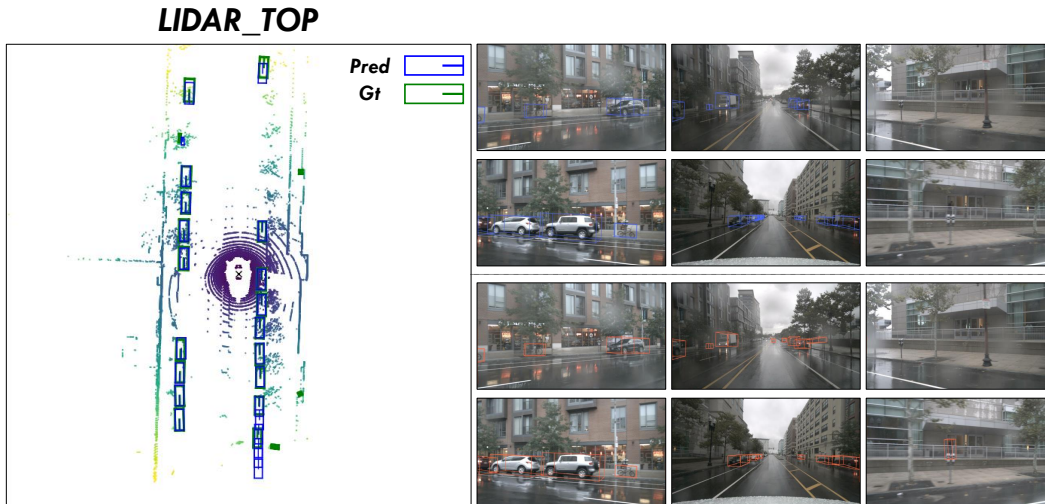


Figure 7: 3D object detection results in BEV and image views. The figure includes the visualization of 3D bounding boxes in different views. The blue boxes in the image views are the prediction results, and the orange boxes are the ground truth.